1. Lithospheric layering in the North American continent from local studies

Our results are consistent with local studies of the fine structure of the upper mantle in those parts of the North American continent where such studies have been conducted. In the Slave craton, petrologic studies[1,2] find two chemically distinct layers in the lithosphere with a boundary between 70 and 150 km and magnetotulleric studies document a highly conductive layer at ~130 km[3,4]). Seismic receiver functions find negative velocity jumps at depths between 90 and 140 km[5-9]. Snyder et al.[9] note a change of anisotropy fabric at 118 km from the transverse component receiver functions beneath the central Slave craton. In the western Superior and the north-western Trans-Hudson Orogen, magnetotulleric studies report conductive anomalies at 80-100 km depth[10,11], similar to those found in the central Slave craton. Receiver functions show a negative velocity gradient at 90 km beneath station FFC[7] and 100 km beneath station ULM in the Trans-Hudson Orogen and western Superior[12], respectively (Fig. 1). *Rychert and Shearer*[7] also report a negative velocity gradient at ~100 km beneath station SCHQ at the boundary between the eastern Superior Province and the New Quebec Orogen. In a surface wave azimuthal anisotropy study of the south-central US, Deschamps et al.[13] report the presence of two layers in the lithosphere near the southern edge of our Layer 1 (their study area is approximately centered at (N36, W85)). Their preferred layer boundary is around 75 km.

2. LAB depth estimates from other studies

The depth of the LAB around 180-240 km in the stable part of the North American continent corresponds well with estimates from other observables, such as shear velocity, electrical resistivity and geochemistry, and in some cases receiver functions. At the continental scale, tomographic images have shown an average of 200-250 km for the lithospheric thickness in the cratonic region[14-17]. Various regional scale studies give more local LAB estimates in the cratonic region. For instance, from tomographic inversion of Rayleigh wave dispersion data, Darbyshire et al.[18] associates the negative velocity gradient at 180-250 km depth beneath the Arctic Canada with the LAB; Chen et al.[19] estimate the LAB at 220 km depth beneath the Slave craton. Geochemistry analysis of Xenoliths data from the northern and Southern Slave craton also gives a depth range of 200-230 km for the LAB[20,21]. Electrical resistivity studies suggest a highly resistive lithosphere with a boundary at 200 km depth beneath the central Slave craton and the Wopmay Orogen in the Northwest Territories, Canada[4,22]. In the central and western Superior Province, lithospheric thicknesses of 140 to 200 km are inferred from Rayleigh

wave phase velocity inversion[23]. A 190-210 km lithosphere thickness is estimated beneath the Superior craton from the major- and trace-element analyses of garnets[2].

References

1 Griffin, W. L. *et al.* Layered Mantle Lithosphere in the Lac de Gras Area, Slave Craton: Composition, Structure and Origin. *J. Petrology* **40**, 705-727, doi:10.1093/petroj/40.5.705 (1999).

2 Griffin, W. L. *et al.* Lithosphere mapping beneath the North American plate. *Lithos* **77**, 873-922 (2004).

3 Jones, A. G., Ferguson, I. J., Chave, A. D., Evans, R. L. & McNeice, G. W. Electric lithosphere of the Slave craton. *Geology* **29**, 423-426, doi:10.1130/0091-7613(2001)029<0423:elotsc>2.0.co;2 (2001).

4 Jones, A. G. *et al.* The electrical structure of the Slave craton. *Lithos* **71**, 505-527 (2003).

5 Yuan, X., Kind, R., Xueqing, L. & Rongjiang, W. The S receiver functions: synthetics and data example. *Geophys. J. Int.* **165**, 555-564 (2006).

6 Bostock, M. G. Mantle stratigraphy and evolution of the Slave Province. *J. Geophys. Res.* **103**, 21,183-121,200 (1998).

7 Rychert, C. A. & Shearer, P. M. A Global View of the Lithosphere-Asthenosphere Boundary. *Science* **324**, 495-498, doi:10.1126/science.1169754 (2009).

8 Moorkamp, M., Jones, A. G. & Eaton, D. W. Joint inversion of teleseismic receiver functions and magnetotelluric data using a genetic algorithm: Are seismic velocities and electrical conductivities compatible? *Geophys. Res. Lett.* **34**, doi:10.1029/2007gl030519 (2007).

9 Snyder, D. B., Rondenay, S., Bostock, M. G. & Lockhart, G. D. Mapping the mantle lithosphere for diamond potential using teleseismic methods. *Lithos* **77**, 859-872, doi:DOI: 10.1016/j.lithos.2004.03.049 (2004).

10 Craven, J. C. *et al.* Conductivity of western Superior Province upper mantle in northwestern Ontario. . *Geological Survey of Canada, Current Research 2001-E6*, 6 (2001).

11 Jones, A. G., Ledo, J. & Ferguson, I. J. Electromagnetic images of the Trans-Hudson orogen: the North American Central Plains anomaly revealed. *Can. J. Earth Sci.* **42(4)**, 457–478 (2005), doi:2010.1139/e2005-2018 (2005).

12 Abt, D. *et al.* North American Lithospheric Discontinuity Structure Imaged By Ps and Sp Receiver Functions. *J. Geophys. Res*, doi:10.1029/2009JB006710 (in press).

13 Deschamps, F., Lebedev, S., Meier, T. & Trampert, J. Stratified seismic anisotropy reveals past and present deformation beneath the East-central United States. *Earth Planet. Sci. Lett.* **274**, 489-498 (2008).

14 Frederiksen, A. W., Bostock, M. G. & Cassidy, J. F. S-wave velocity structure of the Canadian upper mantle. *Phys. Earth and Plan. Int.* **124**, 175-191 (2001).

15 Bedle, H. & van der Lee, S. S velocity variations beneath North America. *J. Geophys. Res.* **114** (2009).

16 Mckenzie, D. & Priestley, K. The influence of lithospheric thickness variations on continental evolution. *Lithos* **102**, 1-11 (2008).

17 Gung, Y., Panning, M. & Romanowicz, B. Global anisotropy and the thickness of continents. *Nature* **422**, 707-711 (2003).

18 Darbyshire, F. A. Upper mantle structure of Arctic Canada from Rayleigh wave dispersion. *Tectonophysics* **405**, 1-23 (2005).

19 Chen, C., Rondenay, S., Weeraratne, D. S. & Snyder, D. B. New constraints on the upper mantle structure of the Slave craton from Rayleigh wave inversion. *Geophys. Res. Lett.* **34**, doi:10.1029/2007GL029535 (2007).

20 Kopylova, M. G. & Russell, J. K. Chemical stratification of cratonic lithosphere: constraints from the Northern Slave craton, Canada. *Earth Planet. Sci. Lett.* **181**, 71-87, doi:Doi: 10.1016/s0012-821x(00)00187-4 (2000).

21 Kopylova, M. G. & Caro, G. Mantle Xenoliths from the Southeastern Slave Craton: Evidence for Chemical Zonation in a Thick, Cold Lithosphere. *J. Petrology* **45**, 1045-1067, doi:10.1093/petrology/egh003 (2004).

22 Spratt, J. E., Jones, A. G., Jackson, V. A., Collins, L. & Avdeeva, A. Lithospheric geometry of the Wopmay orogen from a Slave craton to Bear Province magnetotelluric transect. *J. Geophys. Res.* **114**, doi:10.1029/2007jb005326 (2009).

23 Darbyshire, F. A., Eaton, D. W., Frederiksen, A. W. & Ertolahti, L. New insights into the lithosphere beneath the Superior Province from Rayleigh wave dispersion and receiver function analysis. *Geophys. J. Int.* **169**, 1043-1068 (2007).

24 Wang, Z. & Dahlen, F. A. Spherical-Spline Parameterization of Three-Dimensional Earth Models. *Geophys. Res. Lett.* **22**, doi:10.1029/95gl03080 (1995).

25 Liu, K. H. NA-SWS-1.1: A uniform database of teleseismic shear wave splitting measurements for North America. *Geochem. Geophys. Geosyst.* **10**, doi:10.1029/2009GC002440 (2009).

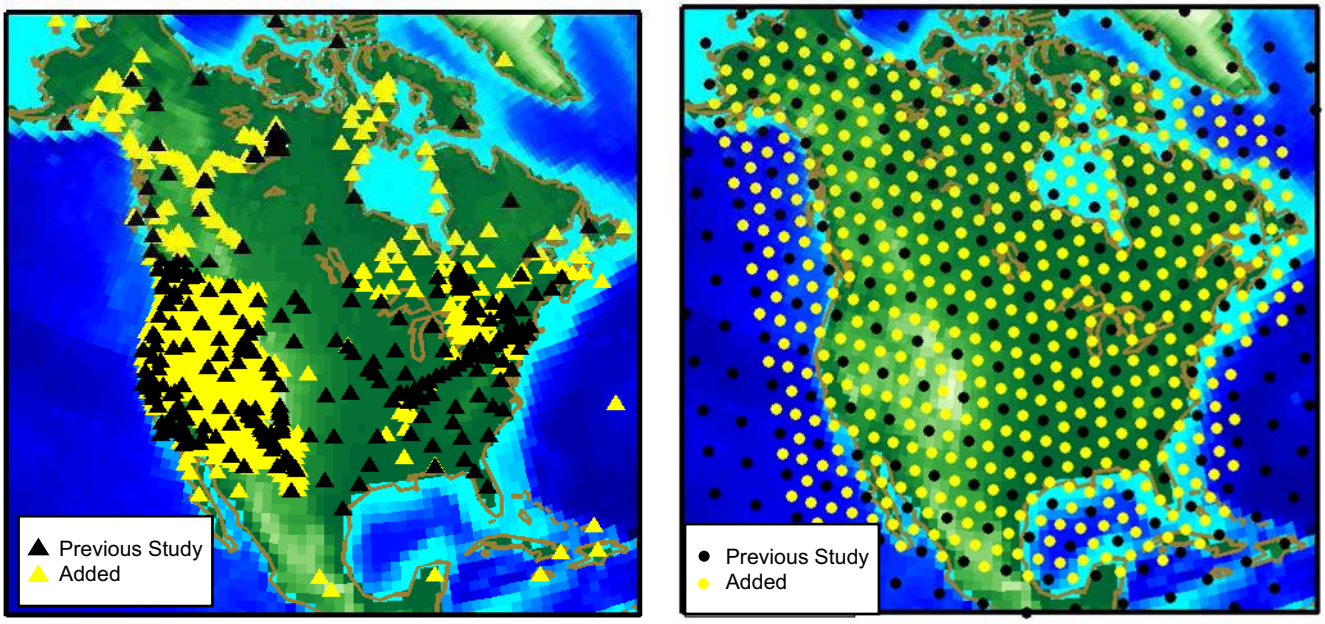

Supplementary Figure 1. Station coverage (a) and model grids (b) used in our inversion for isotropic Vs, radial anisotropy ξ and azimuthal anisotropy G. In (a), black triangles indicate stations used in Paper I, and yellow triangles, stations added in the present study. Transportable array stations and other available broadband stations up to Oct 2008 were used in the current study. This represents three times as many wavepackets as were used in Paper I. For simultaneous Vs and ξ inversion, we used an unconformal spherical spline parameterization[24], as shown in (b). In Paper I we used level 5 (400 km spacing, black dots) for Vs and level 4 (800 km spacing) for ξ and G, respectively. In the present study, we used level 6 (200 km spacing) for Vs, level 5 for ξ and G.

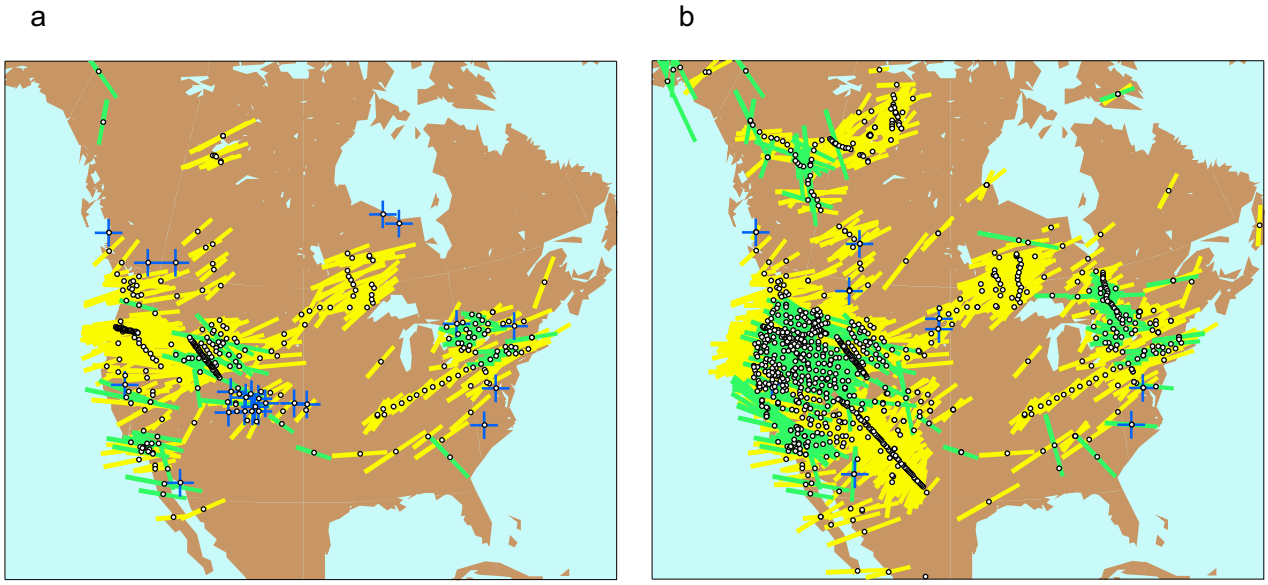

Supplementary Figure 2. SKS splitting dataset used in Paper I (a) and in this study (b).Three times as many SKS splitting data are used in (b) compared to (a). The data are separated into two subsets, for clarity: yellow and green bars show the strength of anisotropy and apparent direction of fast axis from SKS measurements, for apparent fast axis in NE-SW and NW-SE azimuth, respectively. Additional station averaged SKS measurements were compiled from individual databases of Matt Fouch at Arizona State University, Richard Allen at UC Berkeley, Andrew Frederiksen at University of Manitoba, Anna Courtier at James Madison University, and from NA-SWS-1.1[25]. Blue crosses are null measurements. Black dots are stations.

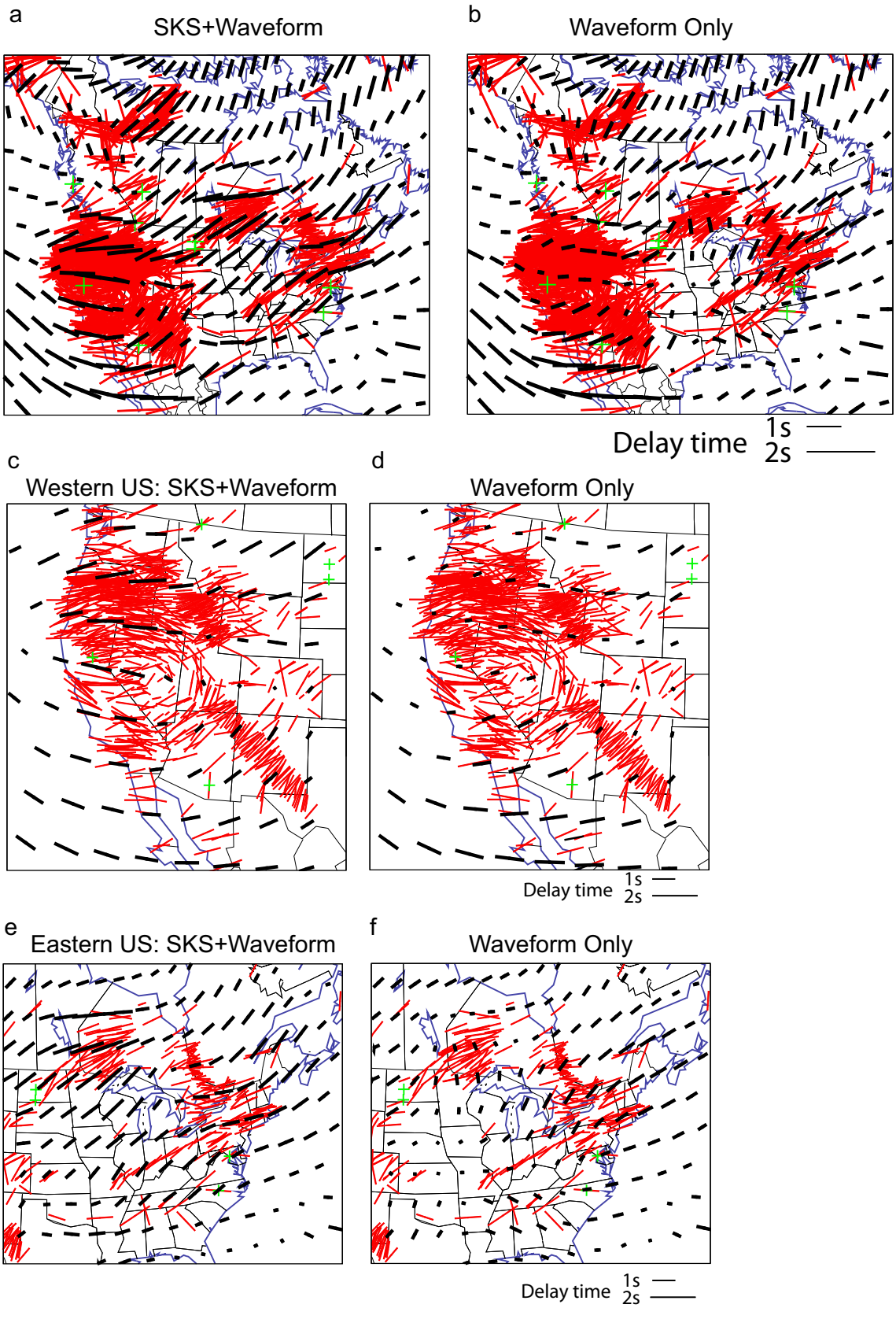

Supplementary Figure 3

Supplementary Figure 3. Observed and predicted SKS splitting from the model derived using waveforms and SKS splitting data (a) and using only waveforms (b). Red bars are SKS splitting measurements, and green crosses are null measurements. Black bars show the predicted average SKS splitting from the two models. (c) and (d) are zoomed views for the western US, and (e) and (f) for the eastern US. Note that the addition of the SKS dataset significantly improves the fits to observed splitting times and fast axis directions, especially in the center of the continent, as is also quantified in the variance reductions shown in Supplementary Figure 4. Supplementary Figure 5 shows that the anisotropy strength recovered at larger depths (> 200 km) when using the combined waveform and SKS dataset is stronger than when using the waveform data alone. Our synthetic tests (Supplementary Figures 6-10) indeed confirm that the addition of SKS data improves the recovery of anisotropy strength at depths larger than 200 km.

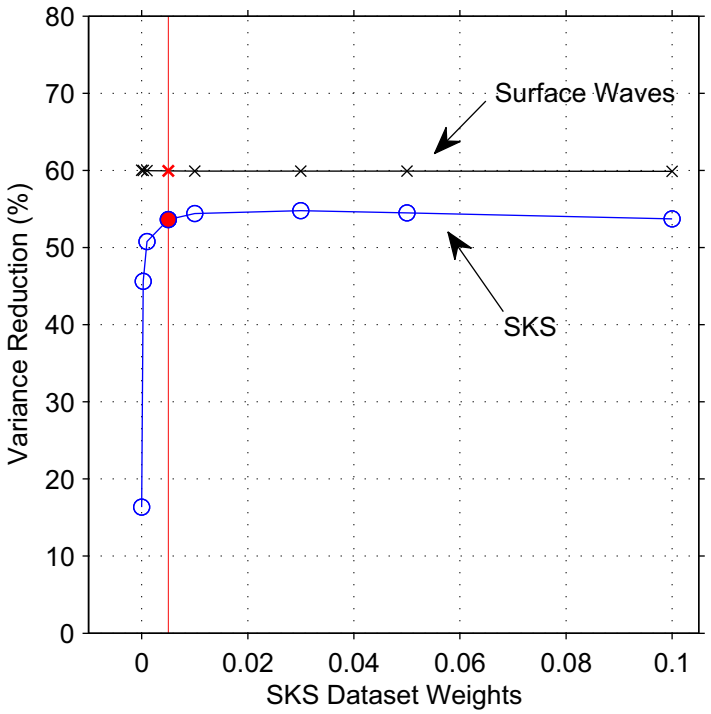

Supplementary Figure 4. Variance reductions for the surface waveform data set (crosses) and SKS splitting data (open circles) as a function of the relative weight of the SKS dataset in the inversion. The amplitude of the weight is not meaningful as it reflects a specific normalization of the kernels. The chosen weight is indicated by the vertical red line.

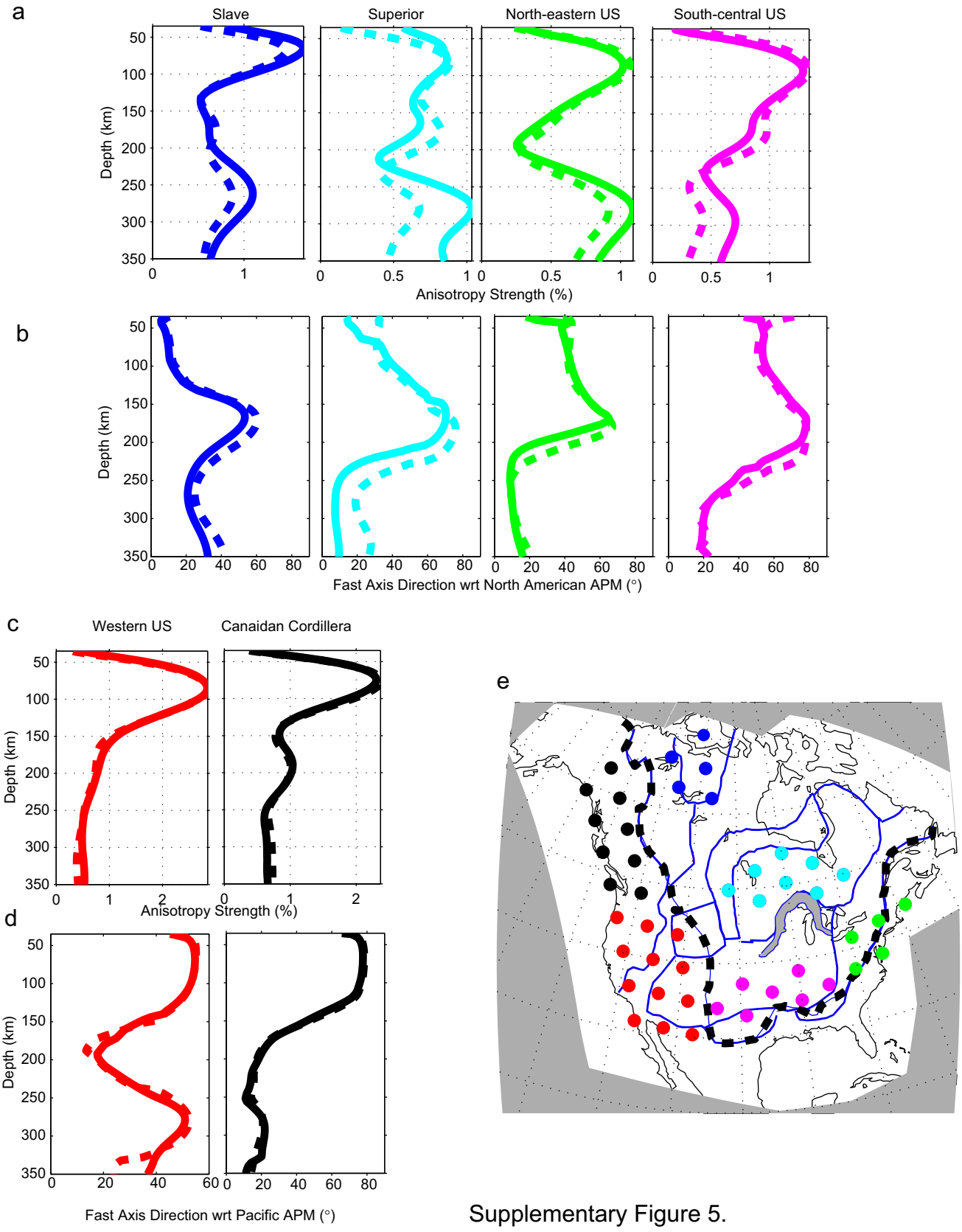

Supplementary Figure 5.

Supplementary Figure 5. Average depth profiles of anisotropy strength (a and c) and fast axis direction (b and d) for 6 subregions of the North American continent, color coded as shown in (e). Broken lines are the results of the inversion using only waveforms, and solid lines are those obtained when SKS splitting data are included. Note that the direction of anisotropy recovered is stable in both cases, whereas the anisotropy strength recovered is larger at depths greater than 200 km for the central parts of the continent, which helps improve the fit to the observed SKS data (Supplementary Figs. 3 and 4). In (a) and (b) the anisotropy direction becomes subparallel to the North American APM below 200 km, with a maximum amplitude around 270 km. Noteworthy is the large anisotropy strength observed at 80-100 km depth in the western US (WUS) (c) and the Canadian Cordillera (d), which corresponds to sub-lithospheric depths. Between 100 and 150 km depth, the fast axis direction rotates from subparallel to the North American APM to a direction closer to the Pacific APM. Deeper in the WUS the fast axis direction shows complexity due to the combined effects of the Pacific APM, current Juan de Fuca subduction, and possibly flows from the northeastern Pacific Rise.

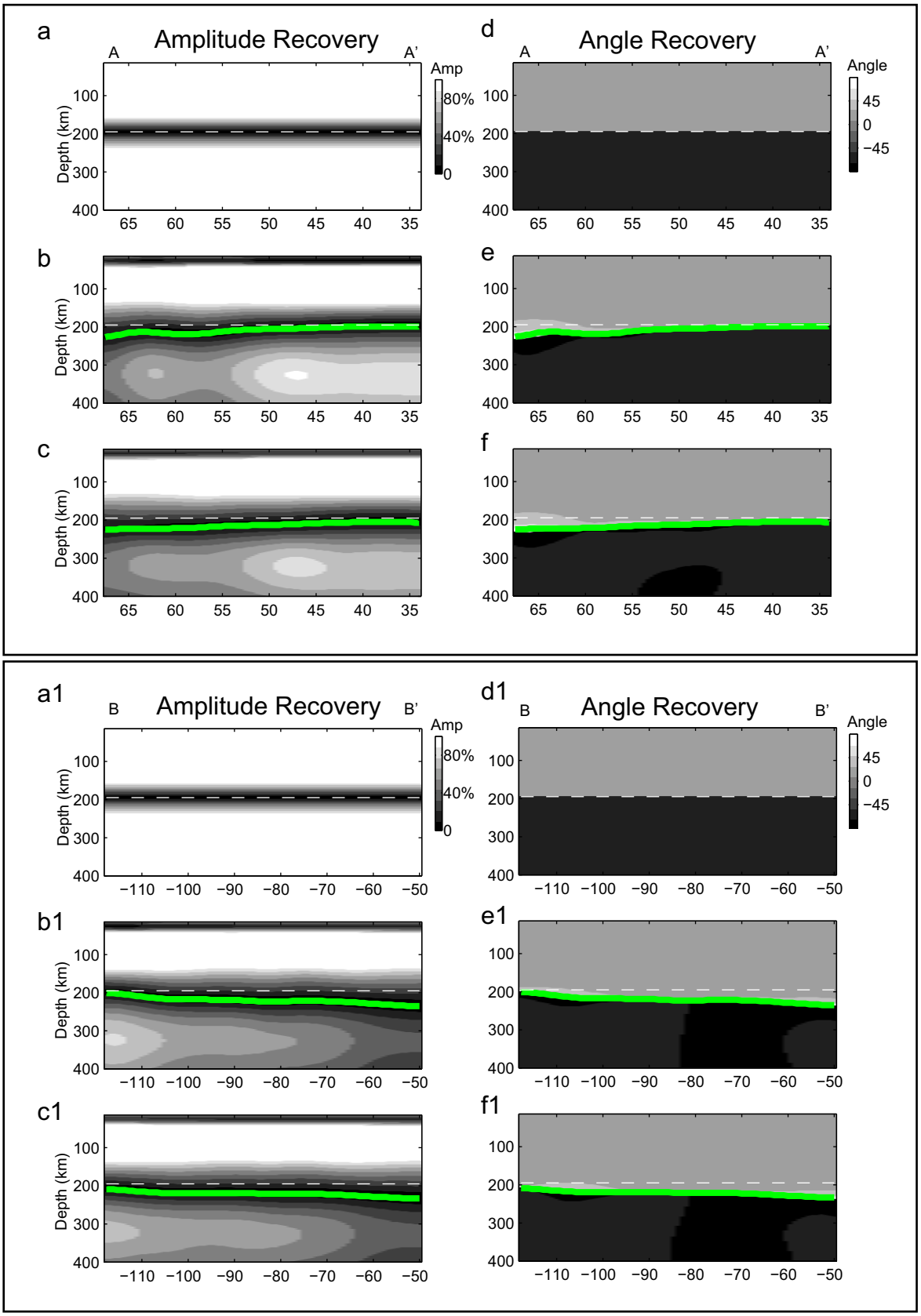

Supplementary Figure 6

Supplementary Figure 6. Resolution tests for a two-layer azimuthal anisotropy model. Top frame: cross-section AA". The left and right sub-panels show results for strength and direction of azimuthal anisotropy, respectively. (a) and (d) Synthetic input model with one layer in the lithosphere and the other in the asthenosphere. The white dashed line marks the fast axis direction change between the layers in the input model. In the left panels (a-c), the strength of anisotropy is shown in gray scale, and in the right panels (d-f), azimuthal anisotropy direction is shaded. (b) and (e): Output model from inversion of combined waveform and SKS datasets. The thick green line is the recovered depth of anisotropy direction change. (c) and (f): Output model from inversion of waveforms only. Both the depth where the anisotropy direction changes and the direction of anisotropy are recovered well. The amplitude of the azimuthal anisotropy is recovered better in the deeper layer when SKS constraints are added. Bottom frame: same as top frame for cross section BB'. Note that BB' runs through regions where the waveform station coverage and SKS measurements are relatively sparse, therefore the recovery of the depth at which the fast axis direction changes is somewhat less accurate.

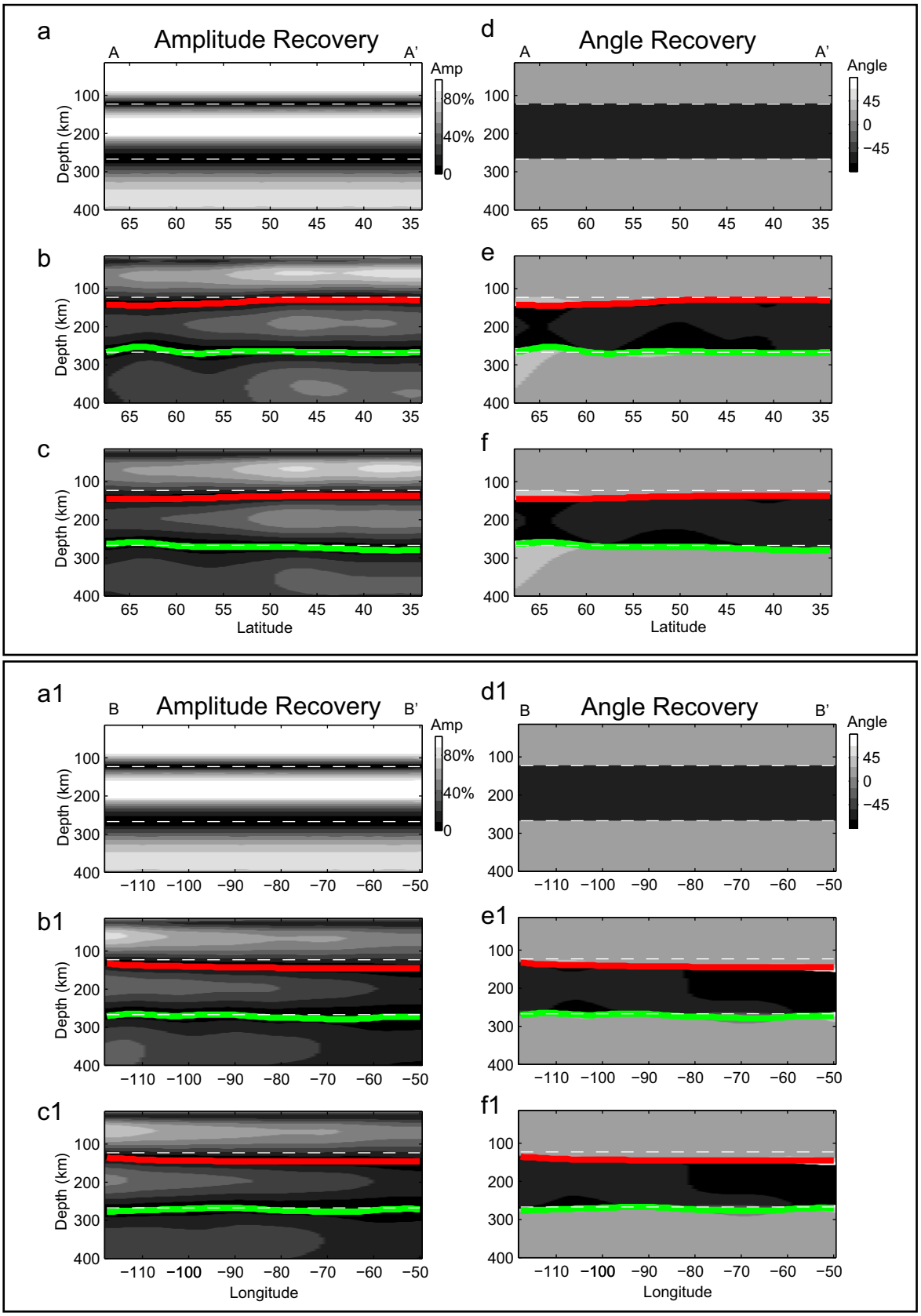

Supplementary Figure 7

Supplementary Figure 7. Same as Supplementary Figure 6 for a three layer input model (a and d), with two layers in the lithosphere and one layer in the asthenosphere. Top frame, cross-section AA'; and bottom frame, cross-section BB'. The green and red lines indicate the depth recovered for the layer 1 and 2 boundaries, respectively. The depth of the change and the direction of anisotropy in all three layers is well recovered. Adding SKS constraints improves the anisotropy amplitude recovery in the lower part of the lithosphere and in the asthenosphere.

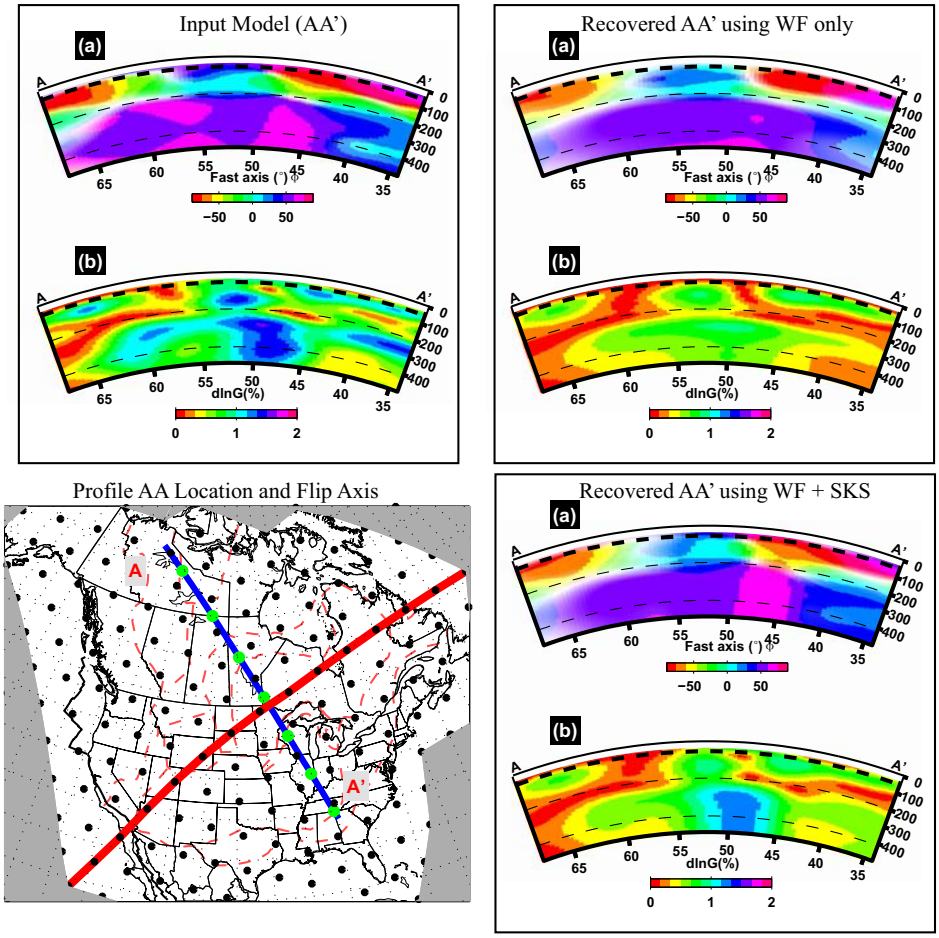

Supplementary Figure 8

Supplementary Figure 8. Resolution test designed to assess the recovery of a realistic azimuthal anisotropy model with comparable lateral and depth variations to our retrieved 3D model. The input model (shown for cross section AA' in the top left panel) is obtained from our final 3-D azimuthal anisotropy model, by flipping the structure by symmetry with respect to the vertical plane indicated in red in the lower left corner map. The lower left panel also shows our model node points in black dots. The right panels are the recovered fast axis directions and the anisotropy strength, using the waveforms only (upper right panel), and combined waveform and SKS datasets (lower right panel). Note the two datasets are both able to recover the changes in fast axis directions in the input model well. Loss of the anisotropy strength is seen in both models, but amplitude recovery is better using the combined waveform and SKS dataset.

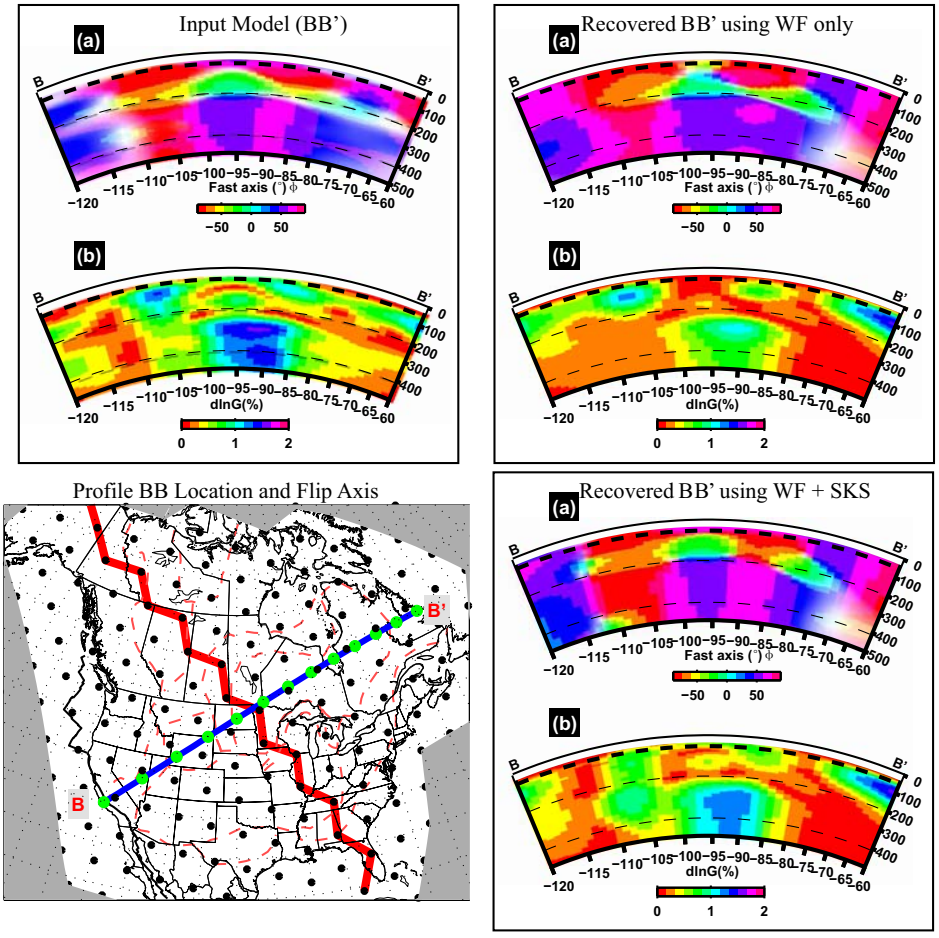

Supplementary Figure 9

Supplementary Figure 9. Same as Supplementary Figure 8 but for another cross-section BB'. The input model is obtained from our final 3D azimuthal anisotropy model by flipping the structure by symmetry with respect to the vertical plane indicated by the red line shown in the map in the lower left panel (this is a different input model than in Supplementary Figure 8). Again the input fast axis directions are recovered very well. And the strength of anisotropy is recovered better when SKS data are included.

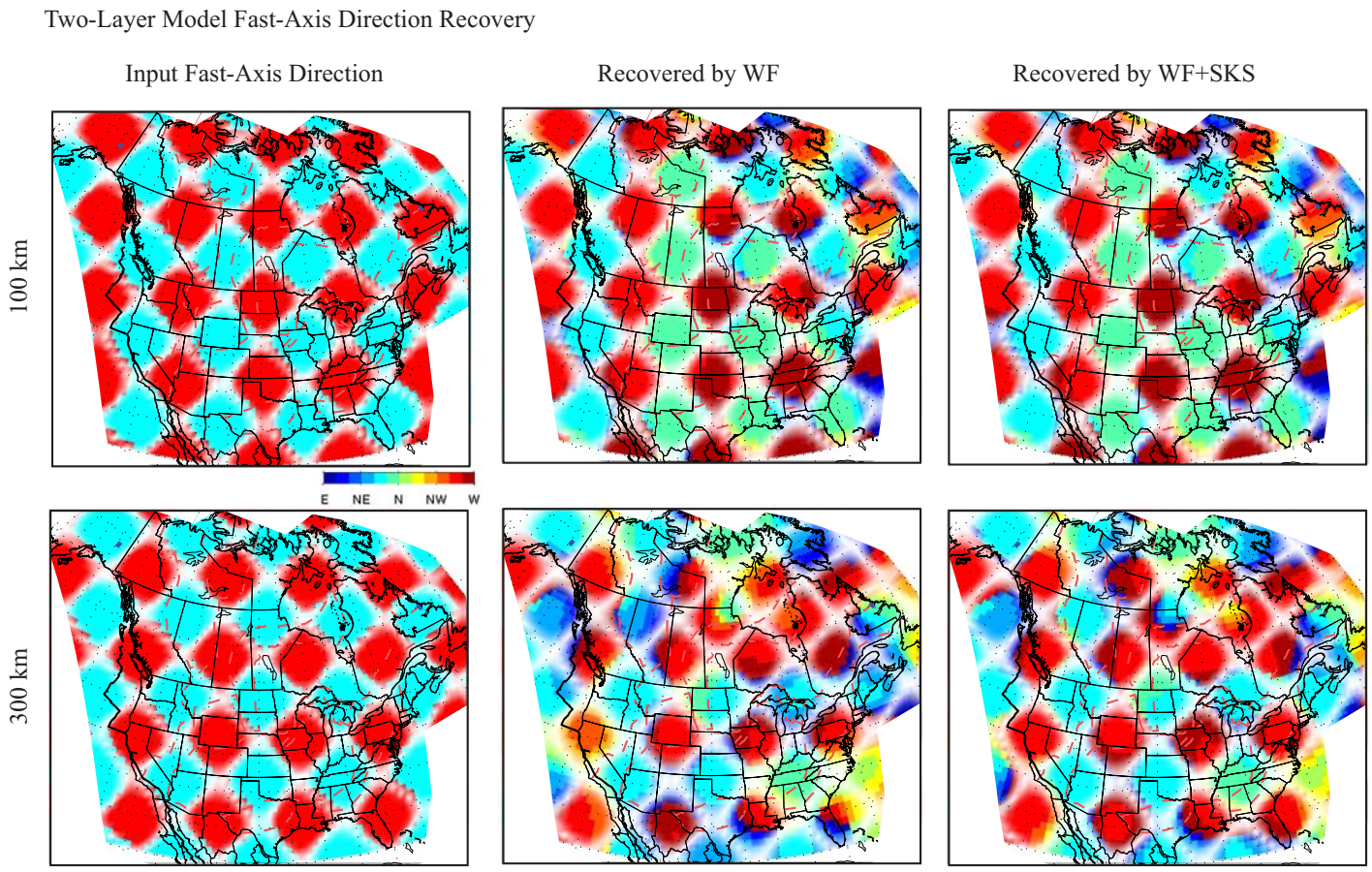

Supplementary Figure 10

Supplementary Figure 10. Two-dimensional checkerboard-like test designed to assess the ability of our data sets to resolve rapid horizontal fast axis changes. The input model (left panels) consists of 7°×7° boxes with alternating fast axis directions (light red and blue) at 100 km and 300 km. Middle panels show output fast axis directions from inversion of the waveforms only. Right panels show output model from inversion of combined waveform and SKS datasets. At 100 km, both datasets recover the rapid fast axis direction changes very well, and in particular in the region corresponding to the Rocky Mountain Front across which our model shows a rapid lateral change in the character of azimuthal anisotropy. The recovery of the fast axis direction is good everywhere at 100 km depth. At 300 km, it is also good, except for the region on the eastern side of Hudson Bay, where some smearing is present, reflecting the sparser distribution of stations in this region. The synthetic tests shown in Supplementary Figures 6 to 10 show that our approach allows us to robustly resolve the vertical layering and rapid horizontal fast axis changes found in our inverted 3D model of azimuthal anisotropy.

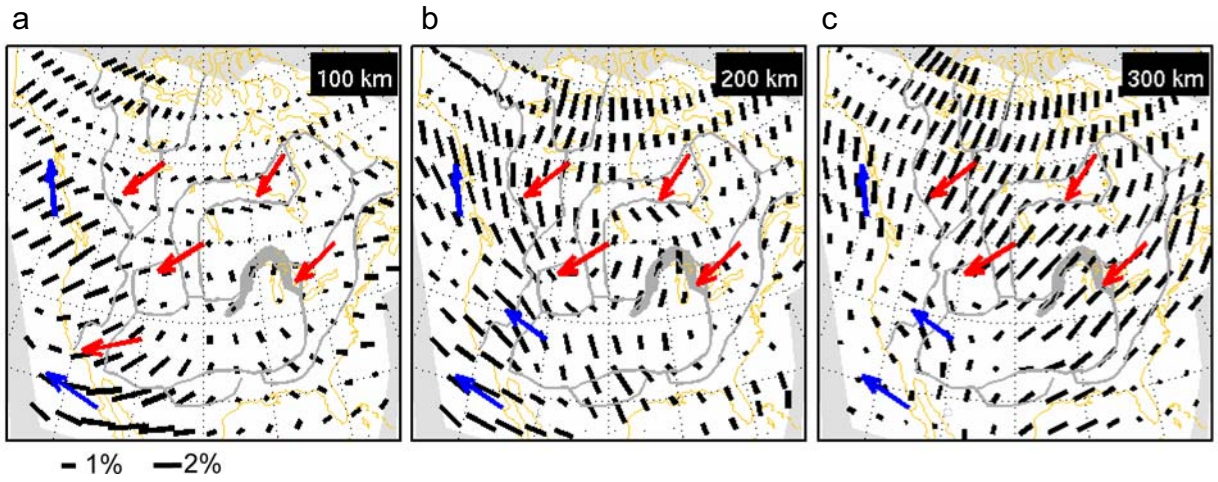

Supplementary Figure 11. Azimuthal anisotropy inversion results at three depths, 100 km, 200 km and 300 km, from left to right, respectively. Black bars show the anisotropy strength and the direction of the fast axis. Red and Blue arrows indicate the direction of the north American and Pacific APM, respectively.

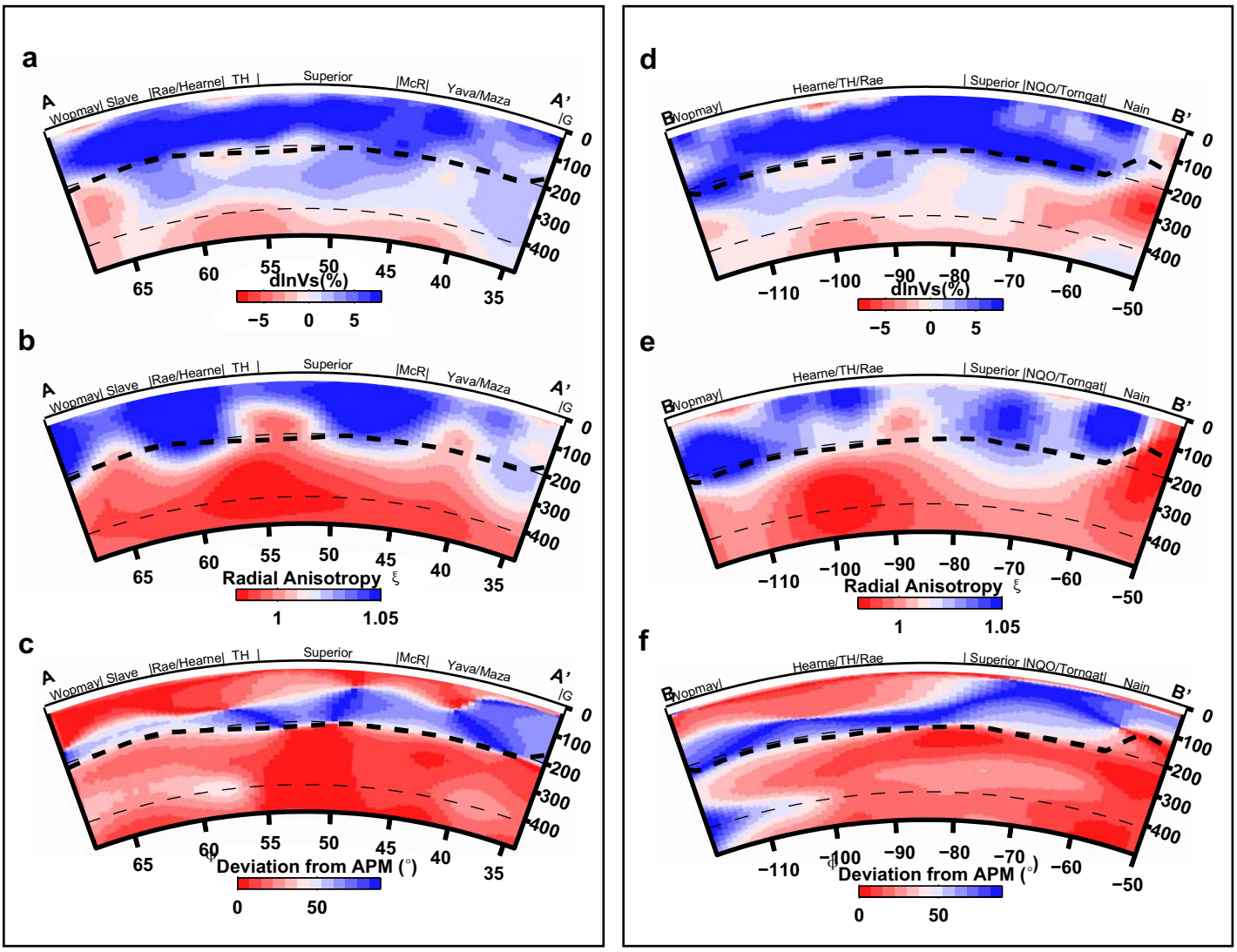

Supplemental Figure 12.

Supplementary Figure 12. Seismic depth cross sections along profiles AA' (left) and BB' (right). See Fig. 1 for the location of AA' and BB'. For each cross section, the three sub-panels are isotropic velocity Vs (a)(d), Radial anisotropy (b)(e), and the fast axis direction with respect to the North American APM (c)(f). Dashed thick black line denotes the LAB estimated from change of direction of the fast axis of anisotropy. Note that it generally corresponds to the zone where isotropic Vs and ξ decrease rapidly with depth. Geological provinces are indicated at the top. Abbreviations are: TH, Trans-Hudson Orogen, McR, the 1.1 Ga Mid-continent Rift; Yava./Maza., the Proterozoic Yavapai and Mazatzal provinces; NQO, New Quebec Orogen. For AA', negative ξ anomalies are observed beneath the Trans-Hudson Orogen (TH) and the Illinois basin (~N40). Significant reduction in ξ is observed across Rae/Hearne and Hearne/Trans-Hudson boundaries, the Trans-Hudson Orogen, and the rifted Nain province. This suggests that, combined with azimuthal anisotropy results, more detailed information about the formation of these lithospheric provinces is contained in the data.